

Dalton Transactions

Accepted Manuscript



This is an *Accepted Manuscript*, which has been through the Royal Society of Chemistry peer review process and has been accepted for publication.

Accepted Manuscripts are published online shortly after acceptance, before technical editing, formatting and proof reading. Using this free service, authors can make their results available to the community, in citable form, before we publish the edited article. We will replace this *Accepted Manuscript* with the edited and formatted *Advance Article* as soon as it is available.

You can find more information about *Accepted Manuscripts* in the [Information for Authors](#).

Please note that technical editing may introduce minor changes to the text and/or graphics, which may alter content. The journal's standard [Terms & Conditions](#) and the [Ethical guidelines](#) still apply. In no event shall the Royal Society of Chemistry be held responsible for any errors or omissions in this *Accepted Manuscript* or any consequences arising from the use of any information it contains.



www.rsc.org/dalton

Cite this: DOI: 10.1039/c0xx00000x

www.rsc.org/xxxxxx

ARTICLE TYPE

Chiral Nematic Mesoporous Films of $\text{ZrO}_2:\text{Eu}^{3+}$: New Luminescent Materials

Guang Chu,^a Jing Feng,^b Yu Wang^{*a}, Xiao Zhang,^c Yan Xu^{*a} and Hongjie Zhang^b

Received (in XXX, XXX) Xth XXXXXXXXXX 20XX, Accepted Xth XXXXXXXXXX 20XX

DOI: 10.1039/b000000x

Integration of luminescent rare earth ions and iridescence into a zirconium oxide photonic material is attractive for the design of new optical devices. The free-standing chiral nematic mesoporous films of $\text{ZrO}_2:\text{Eu}^{3+}$ are assembled by hard-templating approach using nanocrystalline cellulose-templated silica. The $\text{ZrO}_2:\text{Eu}^{3+}$ films show tunable optical properties. The chiral nematic structured $\text{ZrO}_2:\text{Eu}^{3+}$ exhibits selective suppression of the spontaneous emission of Eu^{3+} and the capability to modulate the lifetime of luminescent Eu^{3+} .

Introduction

Incorporation of luminescent species into photonic crystals could modulate their optical properties useful for applications like frequency filters, waveguides, signal modulators, optical switches and fluorescent sensors, *etc.*¹⁻⁴ Photonic crystals have characteristic spatial periodicity in dielectric media on the scale of optical wavelength. Their ability to control electromagnetic waves rivals that of the atomic crystals to manage electrons. Certain rare earth ions exhibit attractive luminescent properties with long emission lifetime and rich emission spectrum. However, these rare earth ions alone are weakly fluorescent due to the parity forbidden f-f transitions. Hosting rare earth ions on photonic crystals may couple the opto-electronic properties of the photonic structures with the luminescent rare earth ions, affording new luminescent materials. Recent work on rare earth-doped photonic crystal including $\text{LiNbO}_3:\text{Yb}^{3+}$, $\text{NaYF}_4:\text{Yb}^{3+}/\text{Er}^{3+}$, $\text{TiO}_2:\text{Er}^{3+}$ and $\text{ZrO}_2:\text{Eu}^{3+}$ are excellent demonstration of this strategy.⁵⁻⁷ Taking $\text{ZrO}_2:\text{Eu}^{3+}$ for example, Song and co-workers report that the structural symmetry around Eu^{3+} and the 3D photonic structure have significant influence on the luminescent properties of inverse opal structured $\text{ZrO}_2:\text{Eu}^{3+}$.

Chiral nematic liquid crystals are 1D photonic crystals, in which mesogens are organized in a helical assembly. The helical organization of a chiral nematic liquid crystal causes angle-dependent selective reflection of circularly polarized light, resulting in iridescence when the helical pitch is of the order of wavelength of visible lights. Since Lord Rayleigh discovered that 1D photonic crystals have high light reflectivity over a well-defined wavelength range known as the stop-band in 1887, 1D photonic crystals have been used for enhancing the efficiency of solar cells, improving the light extraction and color purity of light emitting diodes and optimizing the performance of lasers.¹ For this reason, chiral nematic liquid crystals are drawing increasing

attention for their photonic properties and potential applications in polarizing mirror reflective displays and lasers.^{9, 10}

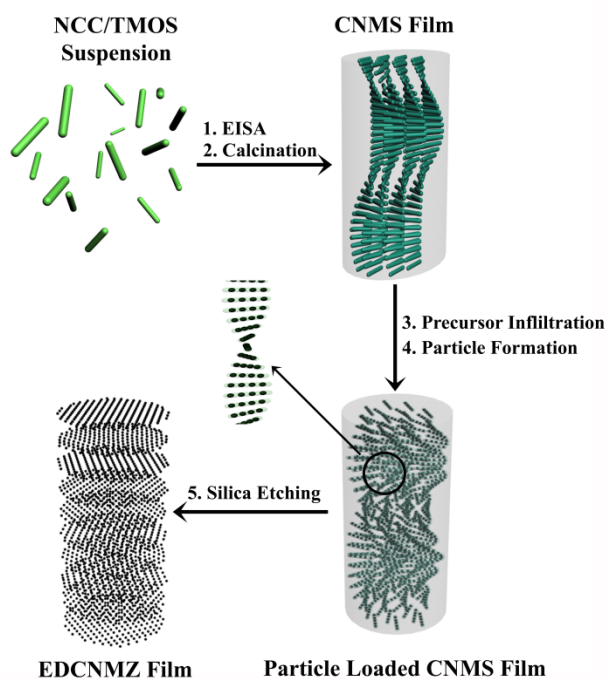
ZrO_2 is considered to be an ideal host matrix for rare earth doping for the fabrication of efficient luminescent materials due to its wide band gap (up to 5.0 eV), good transparency, high refractive index and hardness.¹¹⁻¹⁴ Given that the luminescence of Eu^{3+} is sensitive to surrounding symmetry¹⁵ and the photonic properties of host structures,¹⁶ doping the chiral nematic ordered ZrO_2 with Eu^{3+} may render interesting optical properties and afford new luminescent materials.

Here, we describe the fabrication of chiral nematic mesoporous $\text{ZrO}_2:\text{Eu}^{3+}$ films with tunable helical pitch by a hard-templating approach. Chiral nematic SiO_2 films are prepared by replicating the chiral nematic structure of the nanocrystalline cellulose through an evaporation-induced self-assembly (EISA) pathway and followed by calcination.¹⁷ The helical pitch of chiral nematic SiO_2 is tunable. Free-standing films of chiral nematic mesoporous crystalline $\text{ZrO}_2:\text{Eu}^{3+}$ with specific surface areas of $139.5 \text{ m}^2\text{g}^{-1}$ and strong birefringence are obtained. To the best of our knowledge, this is the first report of its kind that ZrO_2 nanocrystals containing Eu^{3+} ions at lattice sites are organized into a chiral nematic ordering. The luminescent properties of the chiral nematic mesoporous films of $\text{ZrO}_2:\text{Eu}^{3+}$ are studied. We show that chiral nematic ordered $\text{ZrO}_2:\text{Eu}^{3+}$ causes suppression of specific emission lines in a different fashion from the inverse opal structured $\text{ZrO}_2:\text{Eu}^{3+}$.⁸ Such suppression is closely associated with the chiral nematic organization of the ZrO_2 host. The current work provides primary information that the integration of chiral nematic structure with the luminescent rare earth ions renders unique luminescent properties that could be useful in the design and fabrication of new optical devices.

Experimental Section

Materials. All Chemicals were used as received without further purification. Tetramethyl orthosilicate (TMOS, 98%) and europium nitrate hexahydrate ($\text{Eu}(\text{NO}_3)_3 \cdot 6\text{H}_2\text{O}$, 99.9%) were purchased from Aladin Industry corporation. Zirconium oxychloride ($\text{ZrOCl}_2 \cdot 8\text{H}_2\text{O}$, AR) was purchased from Sinopharm Chemical Reagent Ltd. Cotton pulp board was purchased from Hebei Paper Group China.

Preparation of nanocrystalline cellulose (NCC) and chiral nematic mesoporous films of SiO_2 (CNMS). The preparation of NCC and CNMS was done according to the reported



Scheme 1. A schematic diagram of the fabrication of EDCNMZ-n by a hard-templating approach. Calcination was conducted at 600 °C for 6 h.

procedure^{17, 18} and the details of which were provided in the Supporting Information. Two CNMS films with different helical pitch were prepared and used as hard templates, designated as CNMS-S (with short helical pitch) and CNMS-L (with long helical pitch), respectively.

Preparation of chiral nematic mesoporous films of $\text{ZrO}_2\text{:Eu}^{3+}$ (EDCNMZ) and ZrO_2 (CNMZ). The EDCNMZ films were prepared by impregnating CNMS films in a freshly prepared mixed solution containing $\text{ZrOCl}_2\cdot 8\text{H}_2\text{O}$ and $\text{Eu}(\text{NO}_3)_3\cdot 6\text{H}_2\text{O}$ (with the Zr:Eu molar ratio of 199:1, 49:1 and 19:1, respectively) and the total concentration of the mixed solution is 4.0 M. Typically, a piece of CNMS film (105 mg) was dropped into 10 ml mixed solution for 2h until the pores of the CNMS template have been occupied by solution. The salt loaded CNMS film was washed with water to remove the excess salt on the surface of the CNMS film. Next, the impregnated films were dried at 100°C in air for 1 h. Subsequently, it was calcined to induce and facilitate ZrO_2 particles formation and crystallization at 600°C for 6 h. This procedure was repeated four times in total to ensure sufficient pore loading of the CNMS film until the mass of composite film remained constant at 179 mg. Then, the composite film was placed in a 2M NaOH solution (50 ml) for 24h at room temperature to selectively remove the silica template. Finally, the resulting films were recovered by filtration, washed with copious amounts of water, and allowed to air dry giving 76 mg of EDCNMZ film. All the operations were performance under atmosphere. The EDCNMZ films with the Zr:Eu molar ratio of 199:1, 49:1 and 19:1 were designated as EDCNMZ-n (n = 1-3). The CNMZ films without Eu^{3+} doping were prepared using the same procedure as above-mentioned process by immersing a stoichiometric amount of CNMS films in an aqueous solution of

ZrOCl_2 (4 M).

Characterization. Powder X-ray diffraction (XRD) patterns were recorded using a Rigaku D/Max 2550 X-ray diffractometer (Cu K radiation, $\lambda = 1.5406 \text{ \AA}$). Surface morphologies were characterized using JEOL-6700 F field emission scanning electron microscope (SEM) at an accelerating voltage of 3 KV. Transmission electron microscopy (TEM), high resolution transmission electron microscopy (HRTEM) and selected area electronic diffraction (SEAD) analyses were conducted on a FEI Tecnai G2S-Twin with a field emission gun operating at 200 KV. Energy dispersive X-ray (EDX) analysis was performed using a JOEL-IE350 probe. UV-visible spectra were recorded by mounting free-standing films perpendicular to the beam path on a Shimadzu UV-1800 UV-Visible spectrophotometer. Circular dichroism (CD) spectra were recorded on a BioLogic MOS-450 spectropolarimeter and the samples were mounted normal to the beam. Polarized optical microscopy (POM) was conducted on Olympus BX51-P microscope with images taken by polarizers in a perpendicular arrangement. X-ray photoelectron spectroscopy (XPS) was performed on ESCALab 250 Analytical XPS spectrometer with a monochromatic X-ray source (Al $K\alpha$, $h\nu=1486.6 \text{ eV}$). The pressure of the main spectrometer chamber during data acquisition was maintained at 10^{-7} Pa . Nitrogen adsorption-desorption isotherms were recorded at 77.3 K using a Micromeritics ASAP 2420 surface area and porosity analyser and all samples were pretreated at 453K under 10^{-5} Pa , based on which the Brunauer-Emmett-Teller (BET) surface area and Barrett-Joyner-Halenda (BJH) pore size distribution were calculated. Photoluminescence spectra were recorded on FluoroMax-4 fluorescence spectrophotometer (Horiba Scientific) equipped with a 450 W Xe-arc lamp. Emission spectra were corrected for detection and optical spectral response of the spectrofluorimeter and excitation spectra were corrected for the spectral distribution of the lamp intensity using a photodiode reference detector. The luminescent decay curves were recorded on a FLS920 fluorescence spectrometer (Edinburgh Instrument). The excitation source was uF920H Microsecond Flashlamp equipped with a 100W pulse xenon lamp (peak at 395 nm, 2 μs pulse duration, 50 Hz repetition rate).

Results and Discussion

EDCNMZ-n and CNMZ films were fabricated using CNMS as hard templates as illustrated in Scheme 1. Taking EDCNMZ-n for example, an aqueous solution of $\text{ZrOCl}_2\text{-Eu}(\text{NO}_3)_3$ with varying molar ratio of Zr:Eu was loaded into the mesoporous structure of CNMS using the incipient wetness method. The CNMS templates were removed from final composite films using alkaline solution, resulting in free-standing mesoporous films of EDCNMZ-n. The chiral nematic organization, crystal structures and pore profile of EDCNMZ-n are characterized using SEM, XRD and nitrogen adsorption-desorption isotherms, showing that these properties are insensitive to the doping concentration of Eu^{3+} with different Zr/ Eu^{3+} ratio. For ease of discussion, EDCNMZ-1 is used as the representative of EDCNMZ-n. CNMS-S is used as hard-template to fabricate CNMZ and EDCNMZ-n film. CNMS-L is used as template to synthesis EDCNMZ-1'. The UV-Vis and CD spectra

Cite this: DOI: 10.1039/c0xx00000x

www.rsc.org/xxxxxx

ARTICLE TYPE

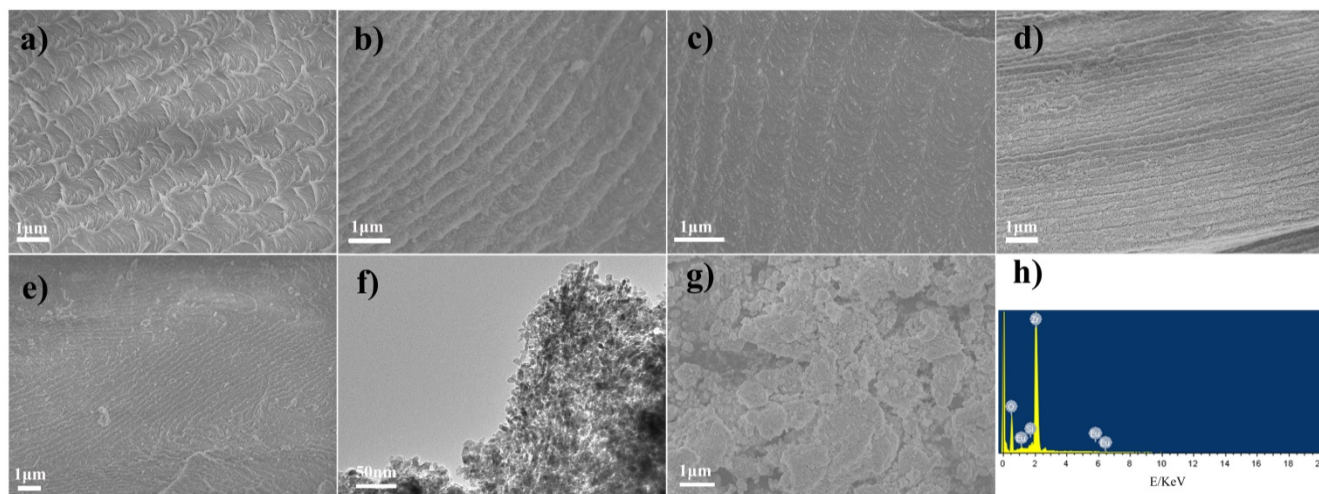


Fig. 1 SEM and TEM images of CNMS, CNMZ, EDCNMZ-1 and REF-1. (a) SEM image of CNMS with a cross-sectional view at high magnification which reveals a left-handed chiral nematic structure. (b) SEM image of CNMZ with a cross-sectional view at high magnification that confirms the transfer of chiral nematic structure from CNMS to CNMZ. (c) SEM image of EDCNMZ-1 with a cross-sectional view at high magnification. (d) SEM image of the side view of EDCNMZ-1 at high magnification shows the stacked layers resulting from the helical pitch of the CNMS template. (e) SEM image of the top view of EDCNMZ-1 at low magnification shows relatively smooth top surface and layered structure. (f) TEM image of EDCNMZ-1 showing the uniform distribution of nanoparticles and inter-nanoparticle void. (g) SEM image of REF-1 showing the absence of helical organization. (h) EDX analysis confirms the presence of Zr and Eu while the presence of Si is negligible in EDCNMZ-1.

of CNMS-S, -L are shown in Fig. S1.

10 Structural Properties of EDCNMZ-1

As shown in Fig. 1a-1c, the ordered helical arrangement of EDCNMZ-1 is evident on the SEM images of all samples, confirming the chiral transfer from CNMS to CNMZ and EDCNMZ-1.^{17, 19} The repeating distance in the order of several

15 hundred nanometers and anti-clockwise twisting morphology are observed, revealing the helical pitch of the chiral nematic phase and the left-handed helical organization in CNMZ and EDCNMZ-1 (Fig. 1b, 1c). The side view of EDCNMZ-1 displays the stacked layers that result from the helical pitch of CNMS (Fig.

20 1d). The top surface of EDCNMZ-1 is relatively smooth, and a layered structure with defects arising from changes in the direction of helical axis of the chiral nematic phase reveals the short-range order of chiral nematic structure (Fig. 1e). TEM image shows that EDCNMZ-1 consists of globular nanoparticles

25 of uniform sizes and textural inter-particle pores of varying sizes (Fig. 1f). We show that it is possible to organize ZrO₂ nanoparticles with and without Eu³⁺ into a macroscopic chiral assembly by replicating multi-length scale structural features, namely nanometer pores, micrometer chiral nematic assembly

30 and centimeter film morphology.²⁰ Crushing EDCNMZ-1 causes a loss of the chiral nematic ordering as indicated by SEM (Fig. 1g). Crushed EDCNMZ-1 is designated as REF-1. Zr (71.94 wt%), O (27.98 wt%) and negligible amount of Si (0.07 wt%) are detected by EDX, indicating the removal of SiO₂ (Fig. 1h).

35 The pore profile of EDCNMZ-1 is examined using nitrogen adsorption-desorption isotherms (Fig. 2a). A typical type IV

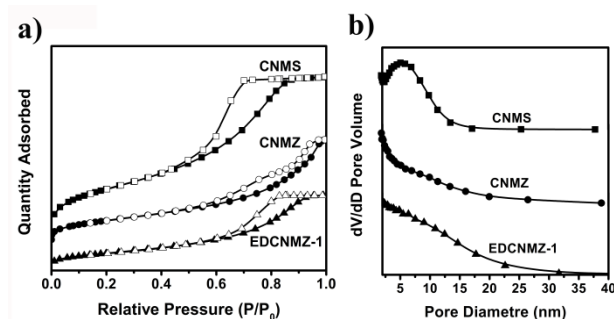


Fig. 2 (a) Nitrogen adsorption-desorption isotherms of CNMS, CNMZ and EDCNMZ-1, respectively. (b) The pore size distributions of CNMS, 40 CNMZ and EDCNMZ-1 based on the BJH model, respectively.

adsorption-desorption isotherm with hysteresis loop in the range of $P/P_o = 0.6 - 0.9$ is observed, suggesting the presence of broad mesopores in EDCNMZ-1 (Fig. 2b). The BET surface area and pore volumes of EDCNMZ-1 are calculated to be 139.5 m² g⁻¹ and 0.27 cm³ g⁻¹, respectively. CNMZ exhibits hysteresis loop at $P/P_o = 0.55 - 1.0$. It contains broad mesopores based on the BJH model with the BET surface area of 182.4 m² g⁻¹ and pore volume of 0.31 cm³ g⁻¹. CNMS exhibits a typical type IV isotherm of mesoporous structure with the BET surface area of 406.9 m² g⁻¹ and pore volume of 0.48 cm³ g⁻¹. Crushing causes a slight change in the porous hierarchy as evidenced by the nitrogen adsorption data between EDCNMZ-1 and REF-1 (Fig. S2).²⁰

The XRD peaks at 30.3°, 35.2°, 50.4° and 60.2° can be indexed to the (111), (200), (220) and (311) diffractions of

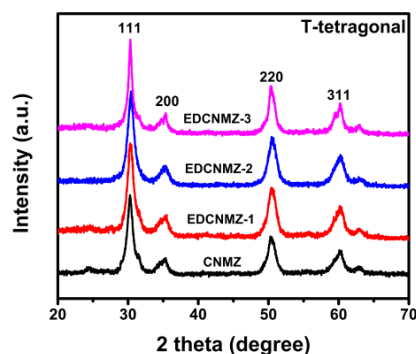


Fig. 3 XRD patterns of EDCNMZ-*n* and CNMZ, showing the tetragonal structure and the absence of crystalline impurity

tetragonal ZrO₂ (JCPDS 50-1089), suggesting both EDCNMZ-*n* and CNMZ have tetragonal symmetry (Fig. 3). No crystalline impurity is found. The peak positions on the XRD patterns of EDCNMZ-*n* and CNMZ are almost identical, suggesting either an *iso*-structural substitution of Eu³⁺ for lattice Zr⁴⁺, given the similar ionic radius of Eu³⁺ (0.094 nm) and Zr⁴⁺ (0.089 nm), or Eu³⁺ existing in amorphous phase which will be discussed at later stage. The average size of EDCNMZ-1 nanoparticles is around 8 nm based on the Scherrer equation, which is in agreement with the observation based on TEM (Fig. 1f). HRTEM shows that EDCNMZ-1 is dominated by crystalline domains with the average *d*-spacing of the lattice fringes around 0.325 nm, agreeing with the *d*₁₂₁ of tetragonal ZrO₂ and the presence of amorphous phase is implied (Fig. S3). The polycrystalline nature of EDCNMZ-1 is revealed by the SAED image (Fig. S3, Inset).

Optical Properties of EDCNMZ-*n*

Chiral nematic structure reflects incident light normal to the surface. The peak wavelength of the reflection, λ_{max}, can be expressed as:

$$\lambda_{\max} = n_{\text{avg}}P \quad (1)$$

where *n*_{avg} is the average refractive index and *P* is the helical pitch of the material.²¹ λ_{max} is a function of *n*_{avg} and *P*, hence,

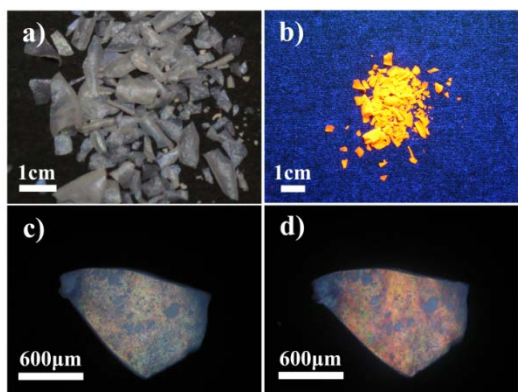


Fig. 4 (a) Photograph of EDCNMZ-1 viewed under natural light shows iridescence. (b) Photograph of EDCNMZ-1 viewed under UV light of wavelength 254 nm shows red emission. (c) POM image of EDCNMZ-1 showing strong birefringence and domains of different orientations. (d) POM image of EDCNMZ-1 after the addition of ethanol showing the change in the birefringence pattern as compared with (c) due to the change in the absorption wavelength λ as a result of changing *n*_{avg}.

tunable by altering either the helical pitch or the average refractive index of the chiral nematic material. EDCNMZ-1 is iridescent and compatible with a chiral nematic structure. As shown in Fig. 4a, EDCNMZ-1 is iridescent, confirming its chiral nematic structure with the helical pitch of the wavelengths of visible light. The EDCNMZ-1 film is luminescent under UV light irradiation (Fig. 4b). POM shows that EDCNMZ-1 is birefringent (Fig. 4c). The birefringence of the mesoporous films of EDCNMZ-1 is changed upon absorption of ethanol due to the change of the average refractive index, *n*_{avg} (Fig. 4d). This change is reversible and the birefringence of the films can be restored upon drying.

The chiral nematic organization of EDCNMZ-1 and CNMZ is further characterized by CD spectra as shown in Fig. 5. It indicates a similar left-handed helical organization.²² The position of the broad CD signal is determined by the helical arrangement of the films, where the shift of the CD signals of EDCNMZ-1 and CNMZ reflect the change in effective *n*_{avg} due to variation of porosity of the two samples. Compared with CNMZ, the CD signal of EDCNMZ-1 is blue-shifted and more intense, indicating a shorter helical pitch (Fig. 5a). EDCNMZ-1 and EDCNMZ-1', which are templated by CNMS-S and CNMS-L, respectively (Fig. S1), adsorb light at different wavelengths (Fig. 5b), reflecting the different helical pitches of the two films which imprinted from the template. The ability to tune the optical properties renders the EDCNMZ films potential uses in the design of smart optical devices.

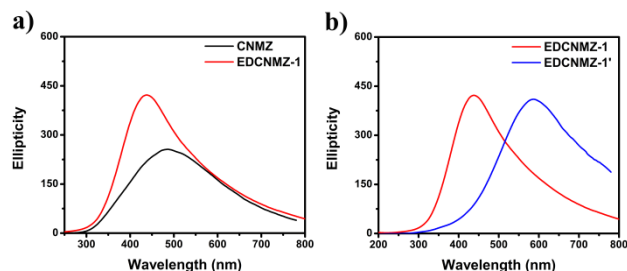


Fig. 5 (a) CD spectra of EDCNMZ-1 and CNMZ. (b) CD spectra of EDCNMZ-1 and EDCNMZ-1' that are templated using CNMS-S and CNMS-L, respectively.

The photoluminescence properties of EDCNMZ-*n* have been studied. Fig. 6 shows the excitation spectra of the films monitored for the emission at 605 nm (the ⁵D₀→⁷F₂ transition of Eu³⁺). The broad bands between 220 nm and 300 nm correspond to the band gap energy of ZrO₂:Eu³⁺, indicating the energy transfer from ZrO₂ nanocrystals to the Eu³⁺ ions. This band is known as charge-transfer band (CTB).²³ According to a commonly accepted mechanism for the energy transfer, the recombination of the electron-hole pairs, generated by the absorbed energy of ZrO₂ nanocrystals, releases energy that is then transferred to the Eu³⁺ ions.

The emission spectra of EDCNMZ-1 and REF-1 were recorded at the wavelength of the absorption of Eu³⁺ at 395 nm and upon excitation into the CTB of Eu³⁺ at 254 nm (Fig. 7). The transitions between 575-650 nm are characteristic of the Eu³⁺ ions. The peaks at 591 nm and 605 nm of EDCNMZ-1 are attributed to the ⁵D₀-⁷F₁ and ⁵D₀-⁷F₂ transition of the Eu³⁺ ions, respectively. It is known that the ⁵D₀-⁷F₁ transition is magnetic-

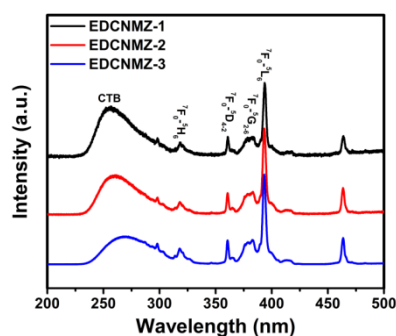


Fig. 6 The normalized excitation spectra of EDCNMZ-*n* (*n*=1-3) monitored at 605 nm. The charge-transfer bands (CTB) redshift and weaken significantly as the Eu^{3+} doping concentration increases.

dipole nature and the crystal field strength around the Eu^{3+} ions have little effect on it. The ${}^5\text{D}_0\text{-}{}^7\text{F}_2$ transition is electric-dipole nature and it is sensitive to the local structure of the Eu^{3+} ions.²⁴ The ratio between the integrated area of the ${}^5\text{D}_0\text{-}{}^7\text{F}_2$ and ${}^5\text{D}_0\text{-}{}^7\text{F}_1$ transitions, labelled as *R*, reflects the local symmetry of the Eu^{3+} ions. Generally, the larger of the *R* value, the lower of the local symmetry. We show that *R* is 1.58 for EDCNMZ-1, 1.66 for EDCNMZ-2 and 1.73 for EDCNMZ-3 ($\lambda_{\text{ex}} = 395$ nm). This indicates that doping of the Eu^{3+} ions causes local disordering, resulting in reduced local symmetry. The higher of the doping concentration of the Eu^{3+} ions, the lower of the local symmetry around Eu^{3+} . Given that Zr^{4+} in the tetragonal ZrO_2 sits on C_{4v} symmetry and Eu^{3+} is slightly larger than Zr^{4+} , the above observation provides evidence for the *iso*-structural substitution of Eu^{3+} for the lattice Zr^{4+} ions. Reduced local symmetry around the Eu^{3+} ions is partially attributed to the local distortion due to the different ionic radius of Zr^{4+} and Eu^{3+} , and partially due to the oxygen vacancy generated by the substitution of Zr^{4+} by Eu^{3+} . The *R* values of REF-*n* are 1.85 for REF-1, 2.05 for REF-2 and 2.20 for REF-3, showing the same trend as those of EDCNMZ-*n*, while the loss of chiral nematic ordering in REF-*n* contributes to the additional reduction of the local symmetry around Eu^{3+} .

It is worth taking note that the ${}^5\text{D}_0\text{-}{}^7\text{F}_1$ transition of REF-1 contains two bands at 591 nm and 596 nm in contrast to the single band at 591 nm of EDCNMZ-1, and the ${}^5\text{D}_0\text{-}{}^7\text{F}_2$ transition of REF-1 contains three bands at 605 nm, 613 nm and 625 nm in contrast to the single band at 605 nm of EDCNMZ-1 (Fig. 7). EDCNMZ-1 and REF-1 have the same tetragonal symmetry (Fig. 3), however, the helical organization is absent in REF-1 (Fig. 1g). The difference between the emission spectra of EDCNMZ-1 and REF-1 may be ascribable to the chiral nematic ordering of EDCNMZ-1 inhibiting the occurrence of the 596 nm, 613 nm and

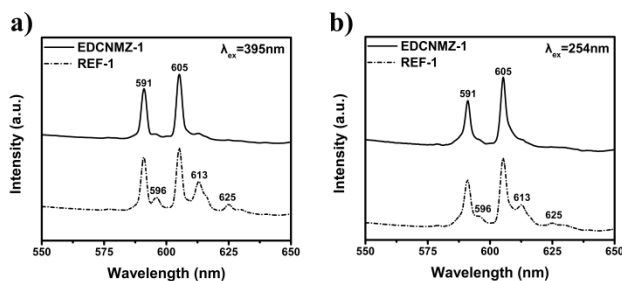


Fig. 7 The normalized emission spectra of EDCNMZ-1 and REF-1 recorded at (a) $\lambda_{\text{ex}} = 395$ nm and (b) $\lambda_{\text{ex}} = 254$ nm

625 nm emissions. The subsequent results show that the lifetimes of REF-1 sample decrease due to disappearance of the chiral nematic mesoporous structure. It implies that the related density of state (DOS) increases with the disappearance of the periodic structure, which confirmed by the previous related reports.^{8, 25, 26} Similar phenomena have also been observed under the excitation at 254 nm (Fig. 7b). The ${}^5\text{D}_0\text{-}{}^7\text{F}_2$ transition at 605 nm should be forbidden when the Eu^{3+} ions sit on the C_{4v} symmetry, however, this does not happen in EDCNMZ-1 implying the local symmetry around Eu^{3+} being distorted.

XPS was performed to characterize the local environment of Eu^{3+} in EDCNMZ-1 and REF-1. As shown in Fig. S4a, the XPS survey spectra of EDCNMZ-1 and REF-1 match well at corresponding binding energies of Eu3d, O1s and Zr3d. The deconvoluted XPS peaks of Eu3d display a quadruplet with bonding energies at 1164.0 eV ($3d_{3/2}$), 1153.8 eV ($3d_{3/2}$), 1134.1 eV ($3d_{5/2}$) and 1124.5 eV ($3d_{5/2}$) (Fig. S4b). The deconvoluted XPS peaks of Zr3d exhibit a doublet at 182.5 eV ($3d_{3/2}$) and 182.5 eV ($3d_{5/2}$) (Fig. S4c). The deconvoluted XPS peaks of O1s are a doublet with binding energies at 530.3 eV and 532.4 eV, which may be attributed to the lattice oxygen and adsorbed oxygen, respectively (Fig. S4d). These results show that Eu^{3+} , Zr^{4+} and O^{2-} have very similar bonding environment in EDCNMZ-1 and REF-1, suggesting that grinding does not change the chemical environment around Eu^{3+} .

The room temperature luminescence decay dynamics of EDCNMZ-1 and REF-1 was monitored for the emissions of 591 nm and 605 nm upon excitation at 395 nm (Fig. 9). The results show that EDCNMZ-1 has longer lifetime than REF-1 for both 591 nm and 605 nm, and the lifetimes of EDCNMZ-1 and REF-1 depend on detected wavelengths that their lifetimes at 605 nm are longer than those at 591 nm. The decay dynamics of EDCNMZ-1 and REF-1 is found to be double-exponential:

$$I(t) = I_1 \exp(-t/\tau_1) + I_2 \exp(-t/\tau_2) \quad (2)$$

where τ_1 and τ_2 are the shorter and longer decay time constants, and I_1 and I_2 are the respective contributions of the shorter and longer decay components. The decay time constants of both samples are obtained by fitting experimental data to the double-exponential function (Table S1). Noticeably, the decay time constants of EDCNMZ-1 are exclusively greater than those of REF-1. Two decay components, τ_1 and τ_2 , indicate two different local environments surrounding Eu^{3+} in EDCNMZ-1 and REF-1, one being ordered and the other being disordered.²⁷ The longer decay time constant corresponds to the Eu^{3+} ions at the ordered site, namely the lattice Eu^{3+} in the host structure of ZrO_2 , and the shorter decay time constant corresponds to the Eu^{3+} ions nearby matrix defects, implying the presence of two Eu^{3+} sites in both EDCNMZ-1 and REF-1. The lifetimes at 591 and 605 nm are different in EDCNMZ-1 and REF-1 samples even though they come from the same excited state. The origins are as follows: (1) the decay time constants vary with monitoring wavelength for all the samples. (2) The different local environments surrounding Eu^{3+} ion should induce different lifetime, being consistent with the previous reports.⁸

EDCNMZ-1 and REF-1 have the same tetragonal structure (Fig. 3) and both are mesoporous (Fig. 2 and Fig. S2). XPS shows that the Eu^{3+} ions have similar chemical environment in both

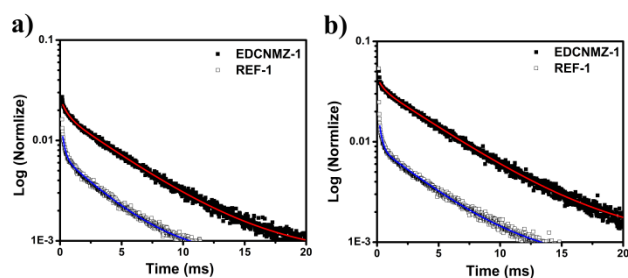


Fig. 8 Room temperature photoluminescence decay curves of EDCNMZ-1 and REF-1 by monitoring the characteristic emissions of (a) 591 nm and (b) 605 nm. Solid lines are experimental curves and dotted lines are fitted curves.

EDCNMZ-1 and REF-1 (Fig. S4). The major difference between EDCNMZ-1 and REF-1 is that the $\text{ZrO}_2\text{:Eu}^{3+}$ nanoparticles are arranged in chiral nematic organization in EDCNMZ-1 (Fig. 1c, 1g). We conclude that the difference between the photoluminescence decay dynamics of EDCNMZ-1 and REF-1 arises mainly from the chiral nematic ordering of EDCNMZ-1. The chiral nematic structure inhibits the spontaneous decay leading to increased fluorescence lifetime. When crushed, the chiral nematic structure disappeared, thus the lifetime of REF-1 decreases. The current contribution demonstrates for the first time that chiral nematic structure can effectively modulate the lifetime of luminescent materials.

Conclusions

Free-standing luminescent films of $\text{ZrO}_2\text{:Eu}^{3+}$ with tunable optical properties and mesoporous structure have been successfully fabricated by using hard templating approach. The chiral nematic structures afford to modulate the spontaneous emission of the Eu^{3+} ions. The emission lines of $^5\text{D}_0\text{-}^7\text{F}_1$ at 596 nm and those of $^5\text{D}_0\text{-}^7\text{F}_2$ at 613 and 625 nm are significantly suppressed and an increase in the luminescence lifetime is observed. The current contribution demonstrates the benefit of integrating luminescence, iridescence and mesoporosity into one free-standing chiral nematic ZrO_2 film. It holds promises for developing new optical nanodevices.

Acknowledgements

The authors are grateful to the funding agencies including the National Natural Science Foundation of China (21171067), Jilin Provincial Talent Funds (802110000412) and Tang Aoqing Professor Funds of Jilin University (450091105161). Sincere gratitude goes to Professor X.Y. Liu for POM imaging analysis and Professor H.W. Song for valuable advises.

Notes and references

^a State Key Lab of Inorganic Synthesis and Preparative Chemistry, Jilin University, 2699 Qianjin Street, Changchun 130012, China;

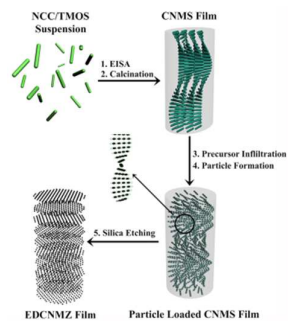
Tel: 86 431 85168607; E-mail: yanxu@jlu.edu.cn

^b State Key Lab of Rare Earth Resource Utilization, Changchun Institute of Applied Chemistry and Chinese Academy of Sciences, Changchun 130022, China.

^c Center of Bioproduct and Bioenergy, Bioproducts, Sciences and Engineering Laboratory, Washington State University, Richland WA 99354-1671, USA.

† Electronic Supplementary Information (ESI) available: [details of any supplementary information available should be included here]. See DOI: 10.1039/b000000x/

- G. von Freymann, V. Kitaev, B. V. Lotsch and G. A. Ozin, *Chem. Soc. Rev.*, 2013, **42**, 2528-2554.
- C.-S. Huang, S. George, M. Lu, V. Chaudhery, R. Tan, R. C. Zangar and B. T. Cunningham, *Anal. Chem.*, 2011, **83**, 1425-1430.
- M. Eichenfield, R. Camacho, J. Chan, K. J. Vahala and O. Painter, *Nature*, 2009, **459**, 550-555.
- E. C. Wu, J. S. Andrew, L. Cheng, W. R. Freeman, L. Pearson and M. J. Sailor, *Biomaterials*, 2011, **32**, 1957-1966.
- A. Ródenas, G. Zhou, D. Jaque and M. Gu, *Adv. Mater.*, 2009, **21**, 3526-3530.
- F. Zhang, Y. Wan, T. Yu, F. Zhang, Y. Shi, S. Xie, Y. Li, L. Xu, B. Tu and D. Zhao, *Angew. Chem. Int. Ed.*, 2007, **46**, 7976-7979.
- F. Zhang, Y. Deng, Y. Shi, R. Zhang and D. Zhao, *J. Mater. Chem.*, 2010, **20**, 3895-3900.
- X. Qu, H. Song, G. Pan, X. Bai, B. Dong, H. Zhao, Q. Dai, H. Zhang, R. Qin and S. Lu, *J. Phys. Chem. C*, 2009, **113**, 5906-5911.
- D. K. Yang, J. West, L. C. Chien and J. Doane, *J. Appl. Phys.*, 1994, **76**, 1331-1333.
- D. Broer, J. Lub and G. Mol, *Nature*, 1995, **378**, 467-469.
- J. Joo, T. Yu, Y. W. Kim, H. M. Park, F. Wu, J. Z. Zhang and T. Hyeon, *J. Am. Chem. Soc.*, 2003, **125**, 6553-6557.
- K. Sato, H. Abe and S. Ohara, *J. Am. Chem. Soc.*, 2010, **132**, 2538-2539.
- B. Liu and R. T. Baker, *J. Mater. Chem.*, 2008, **18**, 5200-5207.
- Y.-S. Ko and Y.-U. Kwon, *ACS Appl. Mater. Inter.*, 2013, **5**, 3599-3606.
- Y. Hui, Y. Zhao, S. Zhao, L. Gu, X. Fan, L. Zhu, B. Zou, Y. Wang and X. Cao, *J. Alloys Compd.*, 2013, **573**, 177-181.
- J. W. Goodby, I. M. Saez, S. J. Cowling, V. Görtz, M. Draper, A. W. Hall, S. Sia, G. Cosquer, S. E. Lee and E. P. Raynes, *Angew. Chem. Int. Ed.*, 2008, **47**, 2754-2787.
- K. E. Shopsowitz, H. Qi, W. Y. Hamad and M. J. MacLachlan, *Nature*, 2010, **468**, 422-425.
- S. Beck-Candanedo, D. Viet and D. G. Gray, *Langmuir*, 2006, **22**, 8690-8695.
- H. Qi, K. E. Shopsowitz, W. Y. Hamad and M. J. MacLachlan, *J. Am. Chem. Soc.*, 2011, **133**, 3728-3731.
- K. E. Shopsowitz, A. Stahl, W. Y. Hamad and M. J. MacLachlan, *Angew. Chem. Int. Ed.*, 2012, **51**, 6886-6890.
- H. de Vries, *Acta Crystallogr.*, 1951, **4**, 219-226.
- M. De Poli, M. De Zotti, J. Raftery, J. A. Aguilar, G. A. Morris and J. Clayden, *J. Org. Chem.*, 2013, **78**, 2248-2255.
- T. Ninjbadgar, G. Garnweitner, A. Börger, L. M. Goldenberg, O. V. Sakhno and J. Stumpe, *Adv. Func. Mater.*, 2009, **19**, 1819-1825.
- Y. Liu, D. Tu, H. Zhu and X. Chen, *Chem. Soc. Rev.*, 2013, **42**, 6924-6958.
- P. Lodahl, A. F. Van Driel, I. S. Nikolaev, A. Irman, K. Overgaag, D. Vanmaekelbergh and W. L. Vos, *Nature*, 2004, **430**, 654-657.
- I. S. Nikolaev, P. Lodahl and W. L. Vos, *J. Phys. Chem. C*, 2008, **112**, 7250-7254.
- P. Ghosh and A. Patra, *Langmuir*, 2006, **22**, 6321-6327.



Hard templating of mesoporous chiral nematic luminescent films of $\text{ZrO}_2:\text{Eu}^{3+}$ (EDCNMZ) with novel emission spectra.